



Research paper

Turbulence measurements at three potential tidal energy sites in the Salish Sea

James R. McVey^a,^{*} Levi Kilcher^{b,c}, Jim Thomson^{d,e}, Zhaoqing Yang^{a,e}^a Pacific Northwest National Laboratory, 1100 Dexter Ave N, Seattle, WA, 98109, United States^b National Renewable Energy Laboratory, 15013 Denver W Pkwy, Golden, CO, 80401, United States^c DeerStone Consulting, 5001 Arctic Blvd #203, Anchorage, AK, 99503, United States^d Applied Physics Laboratory, University of Washington, Seattle, WA, 98195, United States^e Department of Civil and Environmental Engineering, University of Washington, Seattle, WA, 98195, United States

ARTICLE INFO

Keywords:

Salish Sea
Tidal energy
Resource characterization
Turbulence
Hydrodynamic loads

ABSTRACT

Understanding turbulence is critical for the robust design of current energy converters. Subsurface moorings were deployed in the Salish Sea, WA to characterize the turbulence statistics at three potential tidal energy sites: Bellingham Channel, Rosario Strait, and Tacoma Narrows. Measurements were made over two days during spring tides with a combination of acoustic Doppler velocimeters and current profilers in order to analyze the turbulence intensity, integral length scales and turbulent kinetic energy balance. For the four full tidal cycles collected at each site, water velocity peaks at 2.0, 2.8, and 2.5 m/s with average turbulence intensities of 12%, 9%, and 10% for Bellingham Channel, Rosario Strait, and Tacoma Narrows, respectively. The majority of turbulent energy is contained in horizontal anisotropic structures, consistent with the integral length scales observed, and turbulent energy production and dissipation are roughly balanced at the observed sites. Additionally, these channels have significant transverse shear stresses and should not be approximated as wall-bounded flows. This study shows the successful use of buoy-mounted ADVs to gain mid-water column turbulence measurements pertinent to the tidal energy industry, and results from this deployment are important for future work improving a numerical resource characterization model for the Salish Sea.

1. Introduction

The Salish Sea was one of the first major water bodies in the United States to be formally investigated for the suitability of tidal energy harvesting by current energy converters (CECs). Admiralty Inlet, a swift tidal passage that forms the entrance to the Puget Sound, was characterized by a series of field studies in the early 2010s (Gooch et al., 2009; Thomson et al., 2010, 2012; Polagye and Thomson, 2013; Bassett et al., 2013; McCaffrey et al., 2015) and has served as a “test site” for resource characterization procedures in use today (Epler et al., 2010; Palodichuk et al., 2013; Guerra and Thomson, 2017). Admiralty Inlet is not the only potential tidal energy site in the Salish Sea; there are a number of channels located in US waters in the Pacific Northwest that have the potential to support tidal energy long-term and/or be utilized as test sites.

In 2015, the National Oceanographic and Atmospheric Administration (NOAA) began an initiative to improve the network of water level and water velocity stations positioned around the Puget Sound (Kammerer et al., 2021). This initiative included deploying stations in every major channel on the U.S. side of the Salish Sea. These data

are publicly available and accessible from NOAA’s website (National Oceanographic and Atmospheric Administration, 2015). Yang et al. (2021) used these water level and velocity data to validate a numerical model for the specific purpose of identifying potential marine energy sites and quantifying the Salish Sea’s tidal resource.

From this model, three additional sites - Bellingham Channel, Rosario Strait, and the Tacoma Narrows - were found to have enough energy density to initiate further study. While the original model was validated using tide and velocity measurements, turbulence measurements are critical to improving the model’s resolution and accuracy (Yang et al., 2021), particularly for an IEC TS 62600-201 Stage 2 assessment (IEC/TS 62600-201, 2015). Turbulence has already been characterized in Admiralty Inlet (Thomson et al., 2012; Polagye and Thomson, 2013), but this study aimed to analyze turbulence characteristics based on field measurements collected at the three aforementioned locations of interest.

High-fidelity turbulence measurements are typically made with acoustic Doppler velocimeters (ADV), which have superior accuracy to

* Corresponding author.

E-mail address: james.mcvvey@pnnl.gov (J.R. McVey).

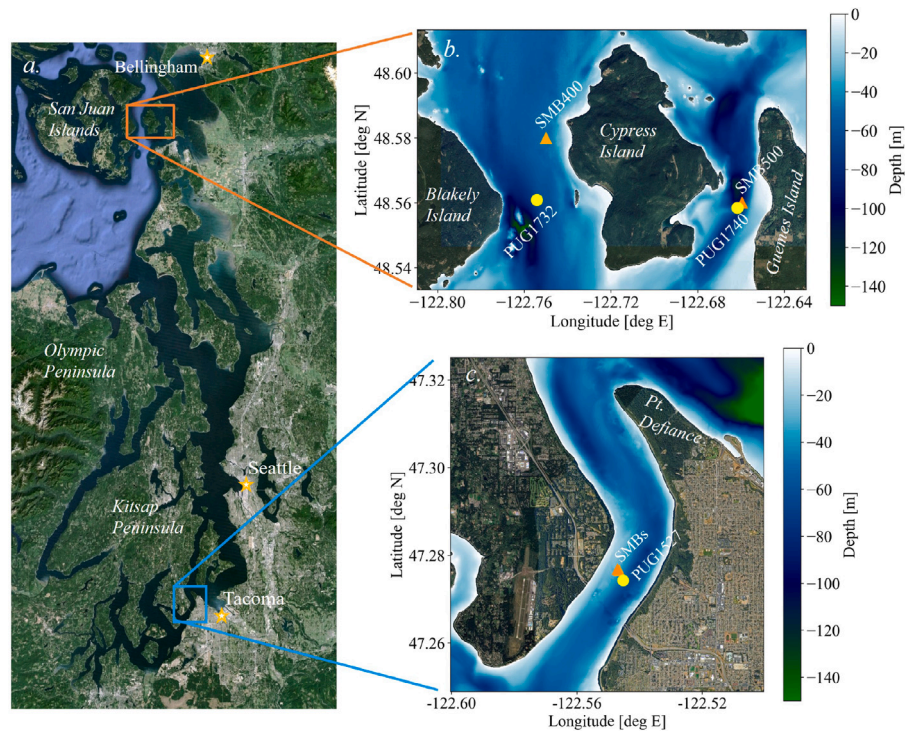


Fig. 1. Map of deployment locations: (a.) image of Puget Sound, WA, USA; (b.) Rosario Strait (left channel) and Bellingham Channel (right channel); and (c.) Tacoma Narrows. The Stablemoor (SMB) moorings are shown by orange triangles, while yellow circles show the NOAA current stations closest to each mooring location.

acoustic Doppler current profilers (ADCPs) (Thomson et al., 2012) but with the tradeoff of taking a point measurement instead of a profile of the water column. ADCPs have since been shown to measure turbulence statistics well if using a high sampling rate (Guerra and Thomson, 2017; Williams and Simpson, 2004), but with some limitations. The 4- and 5-beam instruments must be aligned properly with the principal flow direction; they cannot resolve turbulence scales smaller than their beam spread; and breakdown of the fundamental “assumption of homogeneity” (flow statistics remain unchanged across the beam spread) must not occur (Guerra and Thomson, 2017; Lu and Lueck, 1999; Richmond et al., 2015; Mercier et al., 2021). ADVs, meanwhile, are limited to point measurements, often made from a lander on the seafloor. Combining the use of these two instruments allows the full characterization of a tidal energy site, where the ADCP provides profiles of velocity and shear (e.g., Osalusi et al., 2009), essential for evaluating turbulent kinetic energy production, and the ADV provides high resolution measurements to quantify the turbulence energy budget, intensity, and length scales (e.g., Thomson et al., 2012; Milne et al., 2017). These turbulent statistics are critical for CEC design (Milne et al., 2016).

Positioning an ADV at a height relevant for CECs can be challenging. Previous studies have used tower structures to position an ADV higher in the water column, up to 5 m above the seafloor, though tower vibration can raise instrument noise levels (Thomson et al., 2012; Milne et al., 2013; Gunawan et al., 2014). To get even higher in the water column, at an altitude relevant for utility-scale CECs, Thomson et al. (2015) deployed ADVs on simple spherical floats, termed “Tidal Turbulence Moorings” (TTMs), moored to the seafloor, with decent success. More recently, Harding et al. (2017) and Kilcher et al. (2017b) engineered a method that deployed ADVs on DeepWater Buoyancy Stablemoor buoys, also moored to the seafloor. They showed that compared to the towers and TTMs, the Stablemoor buoys could return higher fidelity ADV measurements if the buoy motion was quantified by both ADCP bottom-track and ADV inertial measurement unit (IMU) measurements. The Salish Sea measurements described here are the third set of resource measurements conducted using the Stablemoor-ADV method, building on lessons learned from the initial Admiralty

Inlet campaign (Harding et al., 2017) and the second set of measurements conducted by the National Renewable Energy Laboratory (NREL) in Western Passage, ME (Kilcher et al., 2017a). These Western Passage measurements were also used for validation of a hydrodynamic and resource characterization model (Deb et al., 2023).

The primary objective of this study was to measure ocean turbulence relevant for CEC design at three Salish Sea sites (Bellingham Channel, Rosario Strait, and the Tacoma Narrows, see Fig. 1) using the Stablemoor-ADV method, and to provide data to further validate the Salish Sea resource characterization model (Yang et al., 2021). Short durations, (i.e., 4 tidal cycles), of data collection were used to meet this objective, since the water velocity at these sites have already been characterized. Spring tides offer the opportunity to capture the full range of turbulence statistics (Milne et al., 2013).

Section 2 of this paper describes the measurement sites and the mooring systems used in this study. Data processing pertaining to the Stablemoor-ADV method is described in Sections 3, and 4 presents the turbulence statistics measured at each of the three sites. Section 5 interprets the results, and Section 6 summarizes the results and future work.

2. Methods

2.1. Site descriptions

In July and November of 2017, mid-water ADV measurements were made using two Stablemoor buoys over a duration of 2–3 days in the Bellingham Channel (BC), Rosario Strait (RS), and the Tacoma Narrows (TN) in the state of Washington, U.S.A (Fig. 1). The particular deployment locations were chosen based on preliminary numerical model analysis of the Salish Sea (Yang et al., 2021) and the proximity to current stations deployed by NOAA in 2015 and 2017 (Kammerer et al., 2021). Deployment locations and NOAA current stations are shown in Fig. 1.

The two Stablemoor buoys utilized in these deployments were designed to carry nose- and wing-mounted ADVs (Harding et al., 2017).

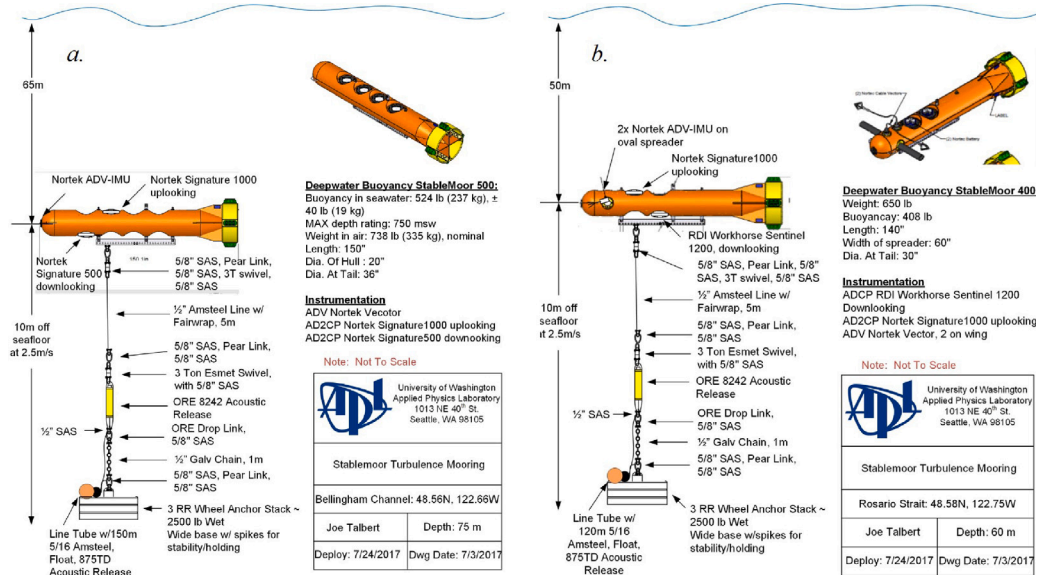


Fig. 2. Stableroos (SMB) mooring drawings, a. Bellingham Channel SMB500, b. Rosario Strait SMB400. Drawings by Joe Talbert (APL-UW).

The Stableroos500 (SMB500, 500 denoting 500 lb of buoyancy) was configured to have a nose-mounted Nortek Vector ADV and instrument wells for additional ADCPs and battery canisters. The Stableroos400 (SMB400) was designed to have dual wing-mounted ADVs located 0.5 m to the port and starboard of the buoy's nose. The Stableroos were moored to 10 m mooring lines and anchored to the seafloor with 1130 kg of wet weight. Two acoustic releases served to recover the mooring: one for the Stableroos and one for the anchor. Both mooring configurations are shown in Fig. 2.

2.1.1. Bellingham channel

Bellingham Channel, located between Guemes and Cypress Islands, WA (Fig. 1b), is around 1.5 km wide at its narrowest and sees maximum tidal flows around 2.5 m/s. The SMB500 was deployed in BC from July 24–27, 2017 at 48.5601 N, 122.6597 W in 86 m of water. This location was approximately 240 m from NOAA station PUG1740 (48.5585 N, 122.6618 W) and is located near a sill between two deeper regions of water to the north and southwest. It was configured with a nose-mounted ADV as well as a down-looking Nortek Signature500 (Sig500) and an up-looking Nortek Signature1000 configured to characterize surface waves. The down-looking ADCP in this case did not have bottom-track.

2.1.2. Rosario strait

Rosario Strait, a deep passage between Cypress Island and the San Jaun Islands, WA (Fig. 1b), to the west, is 2.6 km wide at its narrowest and sees current speeds up to 2.8 m/s. The SMB400 was deployed in RS also from July 24–27, 2017 at 48.5800 N, 122.7501 W in 50 m of water. The closest NOAA station was 2.13 km away, PUG1732 (48.5610 N, 122.7543 W). The chosen deployment site has faster currents than the NOAA station, according to the numerical model (Yang et al., 2021). The SMB400 carried dual wing-mounted ADVs and a down-looking Teledyne RDI Workhorse 1200 (WH1200) with bottom track.

2.1.3. Tacoma Narrows

The SMB500 and SMB400 were redeployed later that year from Nov 14–17, 2017 at a site in the Tacoma Narrows (Fig. 1c). The Tacoma Narrows constricts the Puget Sound tidal prism through a passage that is consistently 1.4 km wide and about 6 km long, and can see maximum tidal flows around 3.5 m/s based on numerical model results (Yang et al., 2021). The moorings were deployed at 47.2769 N, 122.5471 W

and 47.2766 N, 122.5466 W in 32 m of water. The NOAA current station PUG1527 (47.2743 N, 122.5453 W) was located 320 m away.

The SMB500 again held a nose-mounted ADV, but this time utilized a down-looking WH1200 with bottom track and an up-looking Sig500 configured for surface wave characterization. The SMB400 utilized the same configuration as in RS, with dual wing-mounted ADVs and a down-looking WH1200 with bottom track. These Stableroos were deployed within 100 m of each other for instrument redundancy.

2.2. Instrument configurations

The site information and instrument configurations for each Stableroos are given in Table 1. ADVs were set to sample at 16 Hz, following Harding et al. (2017), and the ADCPs were set to sample as fast as possible, with the bottom track instruments recording at 2 Hz. All instruments were internally recording and synchronized with Network Time Protocol (NTP) servers prior to deployment. ADCP bottom track, as well as the IMUs integrated with the ADVs, were used for direct motion correction in post-processing (Kilcher et al., 2017b). A dedicated GPS antenna located above the deployment vessel A-frame's line block was used to maximize the accuracy of the mooring positions.

The following analysis focuses on turbulence measurements from one of the ADVs from each deployment (the nose BC ADV, the RS starboard-wing ADV, and the TN port-wing ADV) and the down-looking ADCP measurements. Bottom track (BT) measurements from the down-looking ADCPs are utilized for motion correction of the velocity measurements.

3. Data processing

Raw data were imported and processed using the Doppler Oceanography Library for pYthon (DOLfYN), now located in the Marine Hydrokinetic Toolkit (MHKiT) (Kluse et al., 2024). Velocity data were quality controlled by removing points with an acoustic signal correlation below 15%, a change in velocity greater than 0.5 m/s in one timestep, and beyond a maximum velocity range of ±3 m/s. Resulting gaps in the ADV signal were replaced with a 10 min average to not affect turbulence statistics (Elgar et al., 2005). The ADV quality controlled data were then motion corrected following the process of Kilcher et al. (2017b).

To apply motion correction, the instrument clocks on each ADV were synchronized to the corresponding down-looking ADCP. To do

so, the down-looking ADCP and the target instrument were rotated from their local coordinate system to one artificially defined for the Stablemoor buoy ($X = \text{forward}$, $Y = \text{port}$, $Z = \text{up}$). With both instruments' data in the same coordinate system, the orientation matrices - tensors defining the instruments' positions in space - were split into 5-min windows and cross-correlated to return a series of time lags representing instrument clock drift at a 5 min interval. The resulting clock drift was then linearly fit and discretized to a resolution of 2 Hz, the BT sampling rate. The ADCP's BT data were rotated into the ADV's coordinate system, mapped onto the ADV's timegrid, subdivided into 5-min windows, and corrected for clock drift.

After time synchronization, the next step was to combine the IMU and BT motion measurements, as the motions measured by the ADV-IMU and BT overlap across a range of frequency bands (Harding et al., 2017). The IMU's accelerometer measures high frequency motion well, but suffers from drift at low frequencies. On the other hand, BT measures low frequency motion well but suffers from noise at high frequencies. Low-frequency drift greatly increases spectral energy at lower frequencies if left unresolved, and BT noise can alter spectral energy at higher frequencies. As such, the IMU velocity measurements are high-pass filtered and the BT velocity measurements are low-pass filtered using a subjectively chosen cutoff frequency and then summed together (Kilcher et al., 2017b).

For the nose-mounted ADVs, high-pass filtering accelerometer data and low-pass filtering BT at 0.1 Hz, rather than the 0.0333 Hz value recommended in Kilcher et al. (2017b), produced the best results in terms of retaining the isotropic turbulence cascade slope in the velocity spectra and minimizing the turbulence parameters that quantify anisotropic turbulence (e.g., Reynolds stresses). For the wing-mounted ADVs, the accelerometer was high-pass filtered at the recommended 0.0333 Hz and BT was low-pass filtered at 0.1 Hz, leaving overlap in the 0.0333 to 0.1 Hz frequency range, in order to properly resolve the velocity spectra. The BC ADV's accelerometer measurements, which did not have available BT, were still low-pass filtered at 0.1 Hz to remove the effects of low-frequency drift.

Velocity data from the down-looking WH1200s were corrected via bottom track measurements and depth bins were mapped based on buoy blowdown, measured by onboard pressure sensors. Velocity data affected by seafloor interference were also removed. Because of the lack of bottom track measurements, the Sig500 data from the BC site were not used in this study.

After motion correction was completed, data were rotated into the principal reference frame (streamwise, cross-stream, up) and divided into subsets (ensembles) of 10 min, based on the IEC TS 62600-201 recommendation (IEC/TS 62600-201, 2015), for further analysis.

4. Measurements

4.1. Water velocity

Water currents in the Salish Sea are predominantly generated by tidal forcing, which varies as one moves inland from the Pacific: they transition from diurnally dominant in the Strait of Juan de Fuca to semidiurnal dominant at Tacoma Narrows (Yang and Wang, 2013). Water velocities measured by the ADVs were compared against NOAA tidal constituent predictions (Parker, 2007) from each location generated by the XTide program (Flater, 2024) and are shown in Fig. 3. Peak water velocities reach 2 m/s at all three sites for the four tidal cycles measured. The BC and RS measurements were taken on the tail end of spring tidal cycles, while TN measurements were recorded mid-tidal cycle in neither spring nor neap tidal exchanges.

Mean ensemble velocity was found to be 38% weaker, based on the percent difference, than the tidal predictions at the BC site, even though the locations were only 240 m apart. This is possibly due to the difference in measurement depth. The NOAA Station PUG1740 was located on the shallowest part of the sill, where the deepest measurements

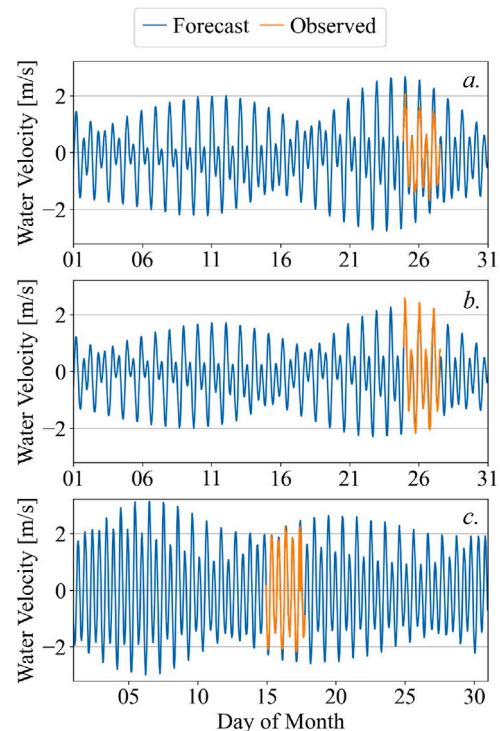


Fig. 3. Forecast vs. observed data in (a.) Bellingham Channel, (b.) Rosario Strait, and (c.) Tacoma Narrows, showing the part of the tidal cycle that measurements were made.

provided are from 36 m (119 ft), while the BC ADV was located slightly off of the sill and recording at 76 m depth. Measurements at Rosario Strait were 11% faster than predictions from Station PUG1732, located over 2 km away. This difference was expected based on the numerical model results (Yang et al., 2021). In this case, the RS ADV was located at 42 m depth, and predictions were taken from 50 m (164 ft). At TN, water velocities were 4% slower as compared to the predictions. The TN ADVs were at a depth of 26 m versus the 21 m (69 ft) prediction from Station PUG1527, 320 m away.

Water velocity and direction from the three ADVs are shown in the form of joint probability plots in Fig. 4. At BC, tidal currents over the measurement interval peak at 1.8 m/s and flow due south on ebb tide and due northeast on flood tide. This change in direction is likely because of channel geometry. The ADV-measured flow was stronger at the RS location, where ebb tide peaks at 2.0 m/s and flood peaks at 2.8 m/s. At RS, flood flows to the north-northwest and ebb to the south-southeast. At TN, the measured tidal currents reach 2.2 m/s. Water current flows parallel to the channel, where ebb tide flows to the north-northeast and flood tide to the south-southwest.

Depth-averaged water velocity and velocity profiles from the down-looking ADCPs at the RS and TN sites are shown in Fig. 5. These profiles show the streamwise water velocity between the Stablemoor buoy and the seafloor. The depth-averaged velocity in the lower 10 m of the water column peaks at 1.5 m/s in both RS and TN for the tidal exchanges measured.

4.2. Velocity spectra

The velocity power spectral densities (spectra) provide valuable information on the structure and distribution of fluid energy. After motion-correcting the velocity vector, spectra were calculated using Welch's method, with a fast Fourier transform (FFT) length equal to one-third of the ensemble window length and using Hanning windowing with 50% overlap (Welch, 1967). Streamwise, transverse and vertical spectra were then binned by their time-averaged flow speed

Table 1
Mooring and instrument configurations.

Mooring	BC SMB500			RS SMB400			TN SMB500			TN SMB400		
Latitude	48.5601			48.5800			47.2769			47.2766		
Longitude	-122.6597			-122.7501			-122.5471			-122.5466		
Water depth [m, MLLW]	86			52			36			36		
Deployment (PST)	2017/07/24 13:58			2017/07/24 14:54			2017/11/14 13:50			2017/11/14 14:04		
Recovery (PST)	2017/07/27 05:35			2017/07/27 06:20			2017/11/17 10:00			2017/11/17 10:10		
Instrument	ADV	Sig500	Sig1000	ADV	ADV	WH1200	ADV	WH1200	Sig500	ADV	ADV	WH1200
Profile direction	-	Down	Up	-	-	Down	-	Down	Up	-	-	Down
Altitude [m]	10	9.75	10.25	10	10	9.75	10	9.75	10.25	10	10	9.75
Fs [Hz]	16	8	8	16	16	2	16	2	8	16	16	2

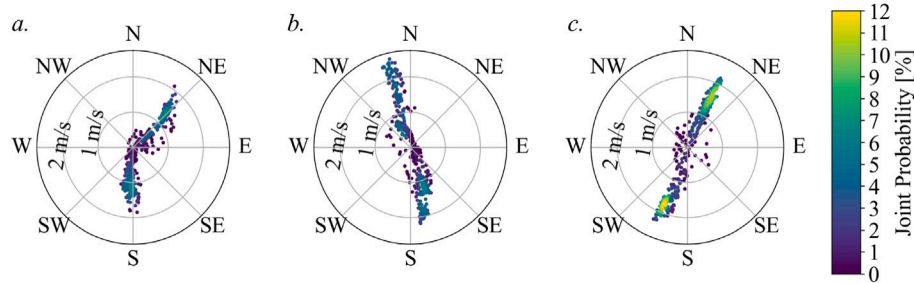


Fig. 4. Joint probability distributions for an ADV located in (a.) Bellingham Channel, (b.) Rosario Strait, and (c.) Tacoma Narrows. Directions are in the “to” convention.

in 0.5 m/s intervals, and spectra from the fastest velocity bin at each site were averaged together and plotted in Fig. 6. The means from the fastest 0.5 m/s-bins at BC, RS, and TN are 1.62, 2.20, and 1.74 m/s, respectively.

The start of the isotropic turbulence cascade, depicted by the characteristic $f^{-5/3}$ slope, can be seen in all three directional spectra at frequencies greater than 0.1–0.2 Hz and up to the instrument noise floors (not shown). Anisotropic turbulence exists at frequencies lower than 0.1 Hz, where energy in the vertical direction falls off relative to the same time-scales in the horizontal directions. Large-scale horizontal turbulent structures are apparent down to frequencies of 0.03 Hz in the RS and TN spectra. These results are consistent with other tidal energy sites (Thiébaud et al., 2020). Below 0.03 Hz, the peak in energy in the streamwise direction occurs at a larger time-scale than both the transverse and vertical directions, suggesting further anisotropy. The vertical motions at low frequencies are likely suppressed by water depth, which provides a strong limit on the vertical extent of turbulence eddies. Notably, similar energy levels can be seen between all three sites, even given the slower flow velocities at BC.

In the BC spectra, the apparent drop in streamwise energy between 0.02 Hz and 0.15 Hz, shaded gray in Fig. 6a, is likely caused by the lack of bottom track measurements necessary for the motion-correction process. Bottom track captures low-frequency motion well, which the onboard IMU cannot do. The lack of motion correction at these frequencies might serve to overestimate transverse turbulent energy and underestimate streamwise turbulent energy in the spectra.

Instrument noise was found from the white noise level in the spectra following Richard et al. (2013) and is around $5 \times 10^{-4} \text{ m}^2/\text{s}^2/\text{Hz}$ in the horizontal directions for all three ADVs. Each instrument’s noise level is used to correct turbulence intensity, Reynolds stresses, and turbulent kinetic energy (TKE) dissipation rates.

Wave energy, which can significantly affect turbulence that CECs deployed near the surface or in shallow waters will experience (Perez et al., 2021), was not observed in the velocity spectra. Wave orbital motion can increase the amplitude of velocity spectra, seen as a sharp increase in energy at the respective wave energy periods (Cossu et al., 2021).

4.3. Turbulence intensity

Turbulence intensity is a basic measure of turbulence that quantifies the variance of fluid velocity and is linked to unsteady loading on

CECs (Milne et al., 2016). It is computed here as the ratio of the noise-corrected standard deviation of water velocity (U) to the mean water velocity (\bar{U}) (Thomson et al., 2012):

$$TI = \frac{\sqrt{(U - \bar{U})^2 - \sigma_n^2}}{\bar{U}}, \quad (1)$$

where instrument Doppler noise (σ_n) was found from the spectral white noise level. Intensities are shown in Fig. 7, with values below 1.0 m/s grayed out, as these are generally below the cut-in speeds for CECs. Flood tide intensities are greater than ebb at the BC and RS sites, likely related to channel geometry and upstream-generated turbulence. At flow speeds above 1 m/s, turbulence intensity averages to 9% during ebb and 14% at flood. During flood and ebb exchanges at RS, intensities average to 10% and 7%, respectively, while at TN, flood and ebb intensities average to 10% for both tides. Turbulence intensity during peak flows in Admiralty Inlet was found to be around 10%, though turbulence intensity during ebb tide was stronger than flood there, which is attributed to a local headland Thomson et al. (2012).

Turbulence intensities at the RS and TN sites show an inverse relationship between turbulence intensity and mean water velocity ($TI \sim 1/\bar{U}$) (Thomson et al., 2012; McCaffrey et al., 2015), though this relationship typically breaks down close to the seafloor. At BC, this inverse relationship holds until a mean water velocity of 0.5 m/s. Beyond 0.5 m/s, the scatter in turbulence intensity suggests there is no correlation between it and mean velocity. The BC ADV is measuring 10 m above the seafloor depth of 86 m (88% depth), so it is reasonable to suspect that bottom effects are more pronounced here.

4.4. Integral length scales

The integral length scales were found from the autocorrelation of the ADV-measured velocity fluctuations, where the integral time scale is estimated by the autocorrelation function integrated from zero to the first zero-crossing lag-time (e.g., McCaffrey et al., 2015; Milne et al., 2013). The integral length scale is then the integral time scale multiplied by the mean ensemble flow speed. The integral time scale is seen as an estimate of the “memory” in the flow, or how long the flow is influenced by (stays correlated with) a perturbation from the mean. The integral length scale is then a corollary estimate of the distance the affected flow travels, and it is often interpreted as the scale of anisotropic turbulence structures.

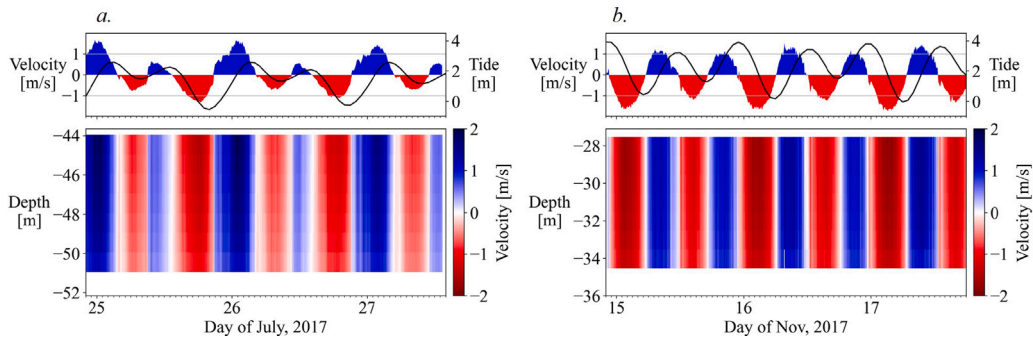


Fig. 5. Water level and velocity profiles from the down-looking WH1200s in (a.) Rosario Strait and (b.) Tacoma Narrows. Top panel shows depth-averaged velocity and water level, and the bottom panel shows the streamwise velocity profile in the bottom 8 m of the water column. The tidal signal here is a progress wave, with velocity preceding water level. Ebb tide is shaded red and flood is shaded blue.

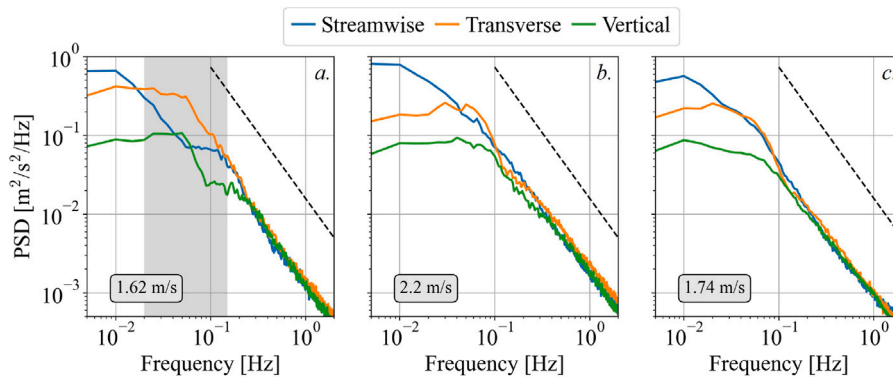


Fig. 6. Power density (velocity) spectra for an ADV located in (a.) Bellingham Channel, (b.) Rosario Strait, and (c.) Tacoma Narrows. The dashed line shows the characteristic $f^{-5/3}$ slope, and the mean water speed for each spectrum is inset in a light gray box. The gray shaded area in (a.) shows the part of the spectrum affected by the lack of motion correction data.

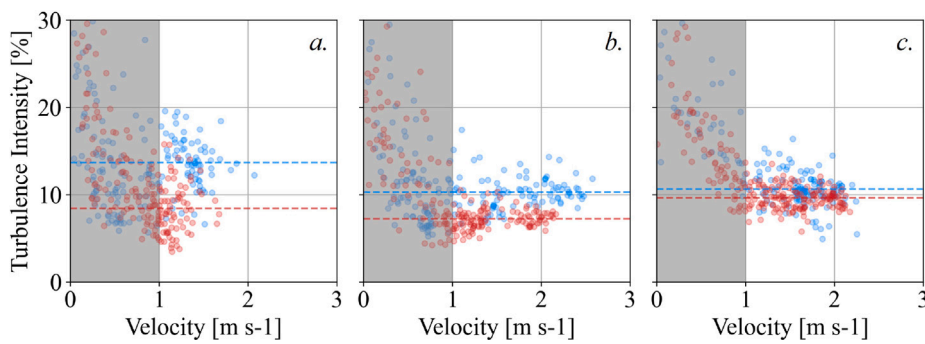


Fig. 7. Turbulence intensity for an ADV located in (a.) Bellingham Channel, (b.) Rosario Strait, and (c.) Tacoma Narrows. Flood tide is shown in blue, and ebb tide is shown in red. The gray region overlays velocity below 1 m/s, a common cut-in speed for tidal turbines.

The integral length scales for the three sites are shown in Fig. 8. The streamwise length scale is largest in RS and smallest in TN, averaging 8.5, 9.3, and 6.9 m, respectively, for BC, RS and TN. The measurement height of 10 m, relative to water depth (z/h), is 12%, 19%, and 28% at BC, RS, and TN, respectively, so these averages are not directly comparable from a hydrodynamic perspective. Nonetheless, at all three sites, the averages are far smaller than the maximums seen. The maximum streamwise integral length scales (75, 121, and 47 m for BC, RS, and TN, respectively) were roughly on the scale of the channels' maximum depths (120, 130, and 50 m, for BC, RS, and RN, respectively), not the depth at the measurement location. Streamwise length scales may be underrepresented at BC, based on the drop in streamwise energy seen in Fig. 6a. In general, compared to the other principal directions, the streamwise length scale is greater than the transverse, which is greater than the vertical.

4.5. Reynolds stresses

The Reynolds stresses ($\overline{u_i u_j}$) parameterize the normal and shear stresses acting on the mean flow, and are calculated from the variance and co-variance of the ADV streamwise (u), transverse (v), and vertical (w) velocity components.

The Reynolds shear stresses $\overline{u'w'}$ and $\overline{v'w'}$ are plotted in Fig. 9, with ebb tide shaded gray. They peak at 1×10^{-2} , 1.5×10^{-2} , and $1.3 \times 10^{-2} \text{ m}^2/\text{s}^2$ (equivalent to 10, 15, and 13 N/m^2) at BC, RS, and TN, respectively. Again, given the drop in spectral energy seen in Fig. 6a due to the lack of bottom track, Reynolds stress estimations are likely underrepresented at the BC site. Still, it appears streamwise and transverse shear stresses are generally equivalent at the BC location, but differ based on the tide at RS and TN. Streamwise shear stress is nearly 10 times stronger than transverse shear stress during flood tide

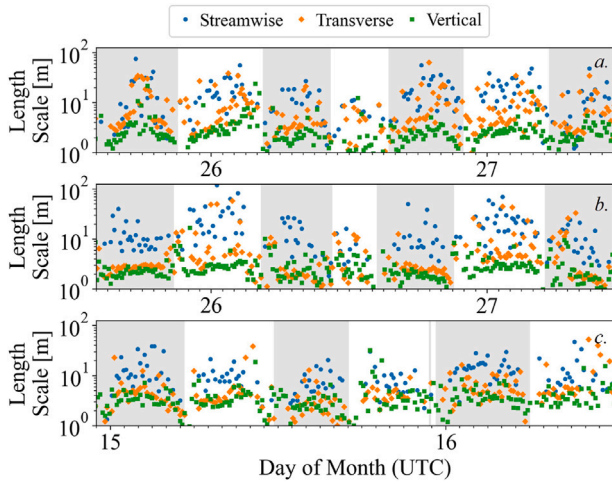


Fig. 8. Integral length scales in the streamwise, transverse, vertical directions from ADV measurements at 10 m above the seafloor in (a.) Bellingham Channel, (b.) Rosario Strait and (c.) Tacoma Narrows. Ebb tide is shaded gray, flood tide is shaded white.

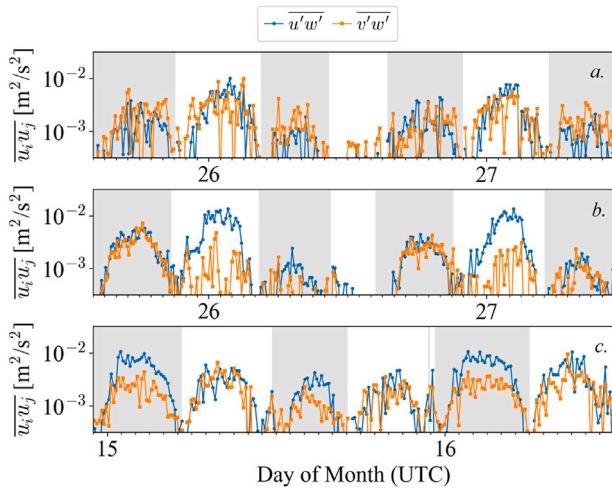


Fig. 9. Magnitude of Reynolds stresses $\overline{u'w'}$ and $\overline{v'w'}$ for an ADV located in (a.) Bellingham Channel, (b.) Rosario Strait, and (c.) Tacoma Narrows. Ebb tide is shaded gray, flood tide is shaded white.

at RS, and it is 5 times stronger during ebb tide at TN, suggesting that these shear flows can be considered wall-bounded only during flood or ebb at each site, respectively. During the opposite tide, these two shear stresses are equivalent and no longer wall-bounded.

The RS deployment location is close to the western shore of Cypress Island, suggesting transverse shear is limited during flood, but current during ebb, coming from open fetch to the NNW, does not yet “feel” this boundary. At TN, it is possible the north-flowing current has conformed to channel width, limiting transverse shear, while the 120 degree channel bend to the north generates transverse shear during the south-flowing flood tide. Turbulence shed from the Tacoma Narrows Bridge during the north-flowing ebb tide is not readily apparent in these measurements, either having dissipated by the time it reached the site or misses the ADV’s location.

4.6. Turbulent kinetic energy balance

TKE production and dissipation represent how much turbulent energy is being produced from the mean flow and subsequently dissipated into heat or sound, and are useful in knowing how much energy is being

drawn from the theoretical tidal resource; this is energy not available to energy harvesting technologies.

4.6.1. Dissipation rate

TKE dissipation rates were calculated from the $f^{-5/3}$ slope of the velocity spectra (Fig. 6) following Lumley and Terray (1983):

$$S(f) = \alpha \epsilon^{2/3} f^{-5/3} \left(\frac{U}{2\pi} \right)^{2/3} + N, \quad (2)$$

where $S(f)$ is the measured spectra, $\alpha = 0.5$, ϵ is the TKE dissipation rate, f is frequency, U is current speed, and N is the Doppler noise level, or white noise floor, of the spectra. Dissipation rates were quality controlled by checking the slope of the spectra found solving for Eq. (2) and comparing it to the expected $f^{-5/3}$ value, $\pm 15\%$, following the QC process of McMillan et al. (2016), McMillan and Hay (2017).

According to Kolmogorov’s “self-similarity” theory, TKE dissipation rate is proportional to U^3/L , where L is the outer length scale, typically equivalent to either water depth or the size of a boundary layer (Kolmogorov, 1941). Within the boundary layer, TKE dissipation and production are expected to be in balance. Outside of the boundary layer, the balance between production and dissipation can be affected by stratification and/or momentum transported past the measurement site.

Dissipation rates at the three sites are shown in Fig. 10. They are roughly similar in magnitude, which is not surprising given the similarity in the energy levels of the isotropic turbulence cascade seen in Fig. 10. Dissipation rates can be seen to follow the U^3/L relationship at RS and TN, while this is not the case at BC, suggesting that dynamics other than bottom boundary layer physics (i.e., lateral processes) are occurring here.

The BC site dissipation rates are stronger at similar flow speeds compared to the RS and TN estimations, consistent with its relatively closer distance to the seafloor. For instance, at 1.5 m/s, the dissipation rate from the BC ADV is estimated to be approximately $3 \times 10^{-4} \text{ m}^2/\text{s}^3$ (equivalent to $0.3 \text{ W}/\text{m}^3$), while it is around half that, $1.5 \times 10^{-4} \text{ m}^2/\text{s}^3$ (equivalent to $0.15 \text{ W}/\text{m}^3$), at the RS and TN ADVs.

There are some differences between ebb and flood tide at both BC and TN, where dissipation rates are slightly weaker (approximately 0.1 decades, or 26%) during ebb than flood. This is possibly due to variability in the local bathymetry and bottom roughness surrounding the sites.

4.6.2. Production rate

TKE shear production rates (P) were estimated using the Reynolds shear stresses from the ADV and the velocity shear gradients from the down-looking ADCP:

$$P = - \left(\overline{u'w'} \frac{\delta \bar{u}}{\delta z} + \overline{v'w'} \frac{\delta \bar{v}}{\delta z} \right). \quad (3)$$

Shear production was found for the RS and TN sites, but it was not estimated at the BC site given the inability to motion-correct its ADCP’s velocity measurements. Buoyancy production is assumed to be negligible at the RS and TN locations, as these sites are generally well mixed, and density stratification in the Salish Sea does not typically vary by tidal cycle (Sutherland et al., 2011; Broatch and MacCready, 2022).

The balance between TKE shear production and dissipation is shown in Fig. 11. At the RS site, production and dissipation are well balanced during both tides, with limited scatter about the 1:1 line, suggesting production is also proportional to U^3/L and that boundary layer physics dominate here. At TN, production and dissipation are roughly balanced during ebb tide, but dissipation is 25%–50% greater than production during flood tide. This suggests that during flood, turbulent energy produced upstream is being transported downstream and dissipated in this part of the channel. It is possible TKE is being generated by the 120 degree channel bend north of the measurement site and is dissipated as the current carries it south.

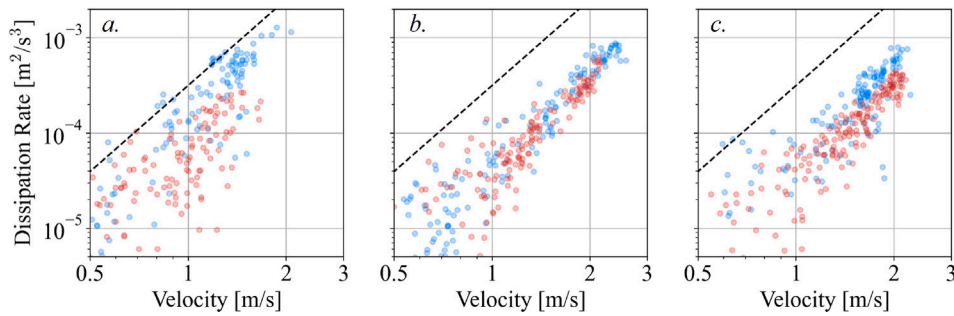


Fig. 10. Dissipation Rate for an ADV located in (a.) Bellingham Channel, (b.) Rosario Strait, and (c.) Tacoma Narrows. Flood tide is shown in blue, and ebb tide is shown in red. The dashed line is the slope of a U^3/L line.

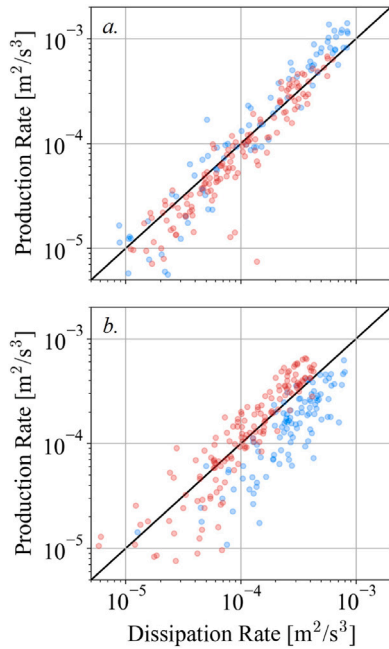


Fig. 11. Balance between TKE shear production rate and dissipation rate in (a.) Rosario Strait and (b.) Tacoma Narrows. Bellingham Channel is not included due to the inability to conduct motion correction. Flood tide is shown in blue, and ebb tide is shown in red. The black line is the 1:1 ratio.

5. Discussion

In this study, turbulence measurements were conducted over the course of 4 tidal exchanges at 3 sites of interest for the marine energy industry. All three site locations had peak currents at or above 2 m/s. Motion correction of the velocity was successful and resulted in velocity spectra comparable to other tidal channels dominated by boundary layer dynamics, where anisotropic turbulence dominates before breaking down into an isotropic turbulence cascade (Thomson et al., 2012; Milne et al., 2013; Gunawan et al., 2014; Thiébaud et al., 2020). Because of these boundary layer dynamics, all three sites show similar turbulence statistics, beneficial for informing structural design decisions for CECs (Milne et al., 2016).

Turbulence intensity describes velocity fluctuation and has a direct effect on CEC power performance and fatigue (Milne et al., 2016; Mycek et al., 2014; Blackmore et al., 2016). In RS and TN they are similar to that seen in Admiralty Inlet (8%–10%) (Thomson et al., 2012), though turbulence intensities in BC are higher because of the buoy’s low relative position in the water column ($z/h = 0.12$).

Integral length scales describe the distance over which turbulence fluctuations are carried by the mean flow. Length scales are attributed

to the magnitude of instantaneous loading on a turbine rotor, even when smaller than the rotor radius (Harrold and Ouro, 2019; Ouro and Stoesser, 2019; Sentchev et al., 2020). A CEC at 10 m above the seafloor can see streamwise integral length scales of at least 10 to 40 m at all three sites. The maximum integral length scales are on the order of the maximum depth of each channel, which is consistent with the results other tidal channels (Thomson et al., 2012; Milne et al., 2017). At the 10 m measurement height, average length scales are similar in magnitude between BC and RS and smaller in the shallower TN.

The Reynolds stresses describe the average transfer rate of momentum via turbulence fluctuations and are useful for the validation of turbulence in numerical models (e.g., Deb et al., 2023). The studied channels do not always exhibit wall-bounded flow, as transverse shear stress ($v'w'$) is on same order as streamwise shear stress ($u'w'$) during ebb tide in RS and flood tide in TN, respectively, and during both tidal exchanges in BC. While narrow channels are typically assumed to be wall-bounded, TN, which is half the width of RS, shows wall-bounded flow during one tidal exchange but not the other, suggesting that other bathymetric features (i.e., headlands) are involved.

TKE shear production and dissipation describe the energy lost to the creation of turbulence fluctuations and the subsequent energy dissipation to viscosity. They increase with both the installation and operation of a turbine in the flow (Guerra and Thomson, 2019). Both are fairly balanced in Rosario Strait, but there is some momentum transport affecting this balance in Tacoma Narrows due to the channel geomorphology or local bathymetric effects.

The Salish Sea, except for the Strait of Juan de Fuca, is protected from swell generated in the Pacific Ocean and lacks a strong wave resource, with wave heights typically below 1.5 m and wave periods below 5 s (Yang et al., 2019). While wave energy was not observed by the ADVs in this study, there is a potential for CECs deployed near the surface at these sites to experience wave orbital fluctuations from wind waves. For example, the theoretical wavelength of a linear, deep-water wave with a 5 s period is 39 m. Assuming wave orbital velocity decays to 0 m/s at a depth of half the wavelength, a 5 s wave’s energy can be detected down to a depth of 19.5 m. That being said, while they can create CEC structural loads (Draycott et al., 2019), waves may not have a strong effect on turbulence statistics (Perez et al., 2021).

These results show the successful implementation of the Stablemoor-ADV method to make high quality measurements of turbulence in the mid-water column. While more deployment intensive than a simple bottom lander, the efficacy of this engineering solution overcomes previous limitations of ADV measurements relevant to the marine energy industry. However, the lack of bottom track measurements on the Bellingham Channel deployment limited the resolution of anisotropic turbulence and likely contributed to the increased variability seen in the results (Kilcher et al., 2017b). Future deployments using the Stablemoor-ADV method should ensure that an ADCP with bottom track is available. It should also be noted that no significant difference in quality was observed between corrected measurements from the

nose- and wing-mounted ADVs in this study, though Harding et al. (2017) observed significant motion in the wing-mounted configuration.

Raw measurements and analyzed data from this study are publicly available on the Marine and Hydrokinetic Data Repository (McVey and Kilcher, 2017). These data will be used to improve the Stage 1 Salish Sea resource characterization model (Yang et al., 2021) to support Stage 2 modeling according to IEC standards (IEC/TS 62600-201, 2015).

6. Conclusions

Measurements, particularly those of turbulence, continue to be important to understanding unsteady load effects on CECs and the relevant fluid–structure interactions. The engineering of utility-scale CECs deployed at these locations will need to take into account turbulence intensities of 7%–14% at peak flow and integral length scales on the order of 10 m. Peak hydrodynamic shear stresses between 10–15 N/m² and energy loss to turbulence from 0.15 to 0.3 W/m³ were also observed at these sites.

All three sites have similar levels of turbulence intensity. Anisotropic turbulence and integral length scales are similar between Bellingham Channel and Rosario Strait, but are smaller in magnitude at Tacoma Narrows, mostly driven by the difference in vertical length scales (i.e. maximum water depth). There are slight differences between Rosario Strait and Tacoma Narrows in terms of momentum transport and the TKE balance, likely due to lateral processes and differences in local bathymetry.

While the Stablemooor-ADV solution is more engineering-intensive in high-velocity flows than that of simple bottom landers, the benefit of collecting simultaneous ADV and ADCP measurements in the mid-water column include fully characterizing the TKE balance and observing smaller turbulence length scales at a height relevant for CECs.

CRediT authorship contribution statement

James R. McVey: Writing – original draft, Visualization, Formal analysis, Data curation. **Levi Kilcher:** Writing – review & editing, Resources, Project administration, Methodology, Investigation, Funding acquisition, Conceptualization. **Jim Thomson:** Writing – review & editing, Resources, Methodology, Investigation, Conceptualization. **Zhaoqing Yang:** Writing – review & editing, Supervision, Project administration, Funding acquisition.

Declaration of competing interest

The authors declare that they have no known competing financial interests or personal relationships that could have appeared to influence the work reported in this paper.

Acknowledgments

The authors would like to thank Joe Talbert and Alex DeKlerk at the University of Washington's Applied Physics Lab for successfully planning and executing the field measurements. We also thank Captain Andy Ellers of the R/V Jack Robertson for the safe and responsive operation of the vessel.

This work was authored by the Pacific Northwest National Laboratory, operated by Battelle Memorial Institute for the U.S. Department of Energy (DOE) under Contract No. DE-AC05-76RL01830; and by the National Renewable Energy Laboratory, operated by Alliance for Sustainable Energy, LLC, for the U.S. DOE under Contract No. DE-AC36-08GO28308. Funding provided by the U.S. Department of Energy Office of Energy Efficiency and Renewable Energy Water Power Technologies Office. The views expressed herein do not necessarily represent the views of the DOE or the U.S. Government. The U.S. Government retains and the publisher, by accepting the article for publication, acknowledges that the U.S. Government retains a nonexclusive, paid-up, irrevocable, worldwide license to publish or reproduce the published form of this work, or allow others to do so, for U.S. Government purposes.

References

- Bassett, C., Thomson, J., Polagye, B., 2013. Sediment-generated noise and bed stress in a tidal channel. *J. Geophys. Res. Ocean.* 118 (4), 2249–2265. <http://dx.doi.org/10.1002/jgrc.20169>.
- Blackmore, T., Myers, L.E., Bahaj, A.S., 2016. Effects of turbulence on tidal turbines: Implications to performance, blade loads, and condition monitoring. *Int. J. Mar. Energy* 14, 1–26. <http://dx.doi.org/10.1016/j.ijome.2016.04.017>.
- Broatch, E.M., MacCready, P., 2022. Mixing in a salinity variance budget of the Salish Sea is controlled by river flow. *J. Phys. Oceanogr.* 52 (10), 2305–2323. <http://dx.doi.org/10.1175/JPO-D-21-0227.1>.
- Cossu, R., Penesis, I., Nader, J.-R., Marsh, P., Perez, L., Couzi, C., Grinham, A., Osman, P., 2021. Tidal energy site characterisation in a large tidal channel in Banks Strait, Tasmania, Australia. *Renew. Energy* 177, 859–870. <http://dx.doi.org/10.1016/j.renene.2021.05.111>.
- Deb, M., Yang, Z., Wang, T., Kilcher, L., 2023. Turbulence modeling to aid tidal energy resource characterization in the Western Passage, Maine, USA. *Renew. Energy* 219, 118694. <http://dx.doi.org/10.1016/j.renene.2023.04.100>.
- Draycott, S., Steynor, J., Nambiar, A., Sellar, B., Venugopal, V., 2019. Experimental assessment of tidal turbine loading from irregular waves over a tidal cycle. *J. Ocean. Eng. Mar. Energy* 5, 173–187. <http://dx.doi.org/10.1007/s40722-019-00136-9>.
- Elgar, S., Raubenheimer, B., Guza, R., 2005. Quality control of acoustic Doppler velocimeter data in the surfzone. *Meas. Sci. Technol.* 16 (10), 1889. <http://dx.doi.org/10.1088/0957-0233/16/10/002>.
- Epler, J., Polagye, B., Thomson, J., 2010. Shipboard acoustic Doppler current profiler surveys to assess tidal current resources. In: *OCEANS 2010. MTS/IEEE*, pp. 1–10. <http://dx.doi.org/10.1109/OCEANS.2010.5664387>.
- Flater, D., 2024. XTide version 2.15.5.
- Gooch, S., Thomson, J., Polagye, B., Meggitt, D., 2009. Site characterization for tidal power. In: *OCEANS 2009. IEEE*, pp. 1–10. <http://dx.doi.org/10.23919/OCEANS.2009.5422134>.
- Guerra, M., Thomson, J., 2017. Turbulence measurements from five-beam acoustic Doppler current profilers. *J. Atmos. Ocean. Technol.* 34 (6), 1267–1284. <http://dx.doi.org/10.1175/JTECH-D-16-0148.1>.
- Guerra, M., Thomson, J., 2019. Wake measurements from a hydrokinetic river turbine. *Renew. Energy* 139, 483–495. <http://dx.doi.org/10.1016/j.renene.2019.02.052>.
- Gunawan, B., Neary, V.S., Colby, J., 2014. Tidal energy site resource assessment in the East River tidal strait, near Roosevelt Island, New York, New York. *Renew. Energy* 71, 509–517. <http://dx.doi.org/10.1016/j.renene.2014.06.002>.
- Harding, S., Kilcher, L., Thomson, J., 2017. Turbulence measurements from compliant moorings. Part I: Motion characterization. *J. Atmos. Ocean. Technol.* 34 (6), 1235–1247. <http://dx.doi.org/10.1175/JTECH-D-16-0189.1>.
- Harrold, M., Ouro, P., 2019. Rotor loading characteristics of a full-scale tidal turbine. *Energies* 12 (6), 1035. <http://dx.doi.org/10.3390/en12061035>.
- IEC/TS 62600-201, 2015. Tidal Energy Resource Assessment and Characterization. International Electrotechnical Commission, URL: <https://webstore.iec.ch/publication/22099>. (Accessed 1 July 2020).
- Kammerer, C., Dusek, G., Heilman, L., Kirk, K., Paternostro, C., 2021. Puget Sound Current Survey 2015–2017, Including the United States' Portions of the Greater Salish Sea. Technical Report, National Oceanic and Atmospheric Administration, <http://dx.doi.org/10.25923/ba7d-v223>.
- Kilcher, L., Fogarty, M., Anderton, S., 2017a. 2017 western passage tidal energy resource characterization measurements. <http://dx.doi.org/10.15473/1635227>, URL: <https://mhkdr.openei.org/submissions/323>.
- Kilcher, L.F., Thomson, J., Harding, S., Nylund, S., 2017b. Turbulence measurements from compliant moorings. Part II: Motion correction. *J. Atmos. Ocean. Technol.* 34 (6), 1249–1266. <http://dx.doi.org/10.1175/JTECH-D-16-0213.1>.
- Klise, K., Pauly, R., Ruehl, K.M., Olson, S., Shippert, T., Morrell, Z., Bredin, S., McVey, J., Lansing, C., Macduff, M., Martin, T., Sivaraman, C., Gunawan, B., Driscoll, F., 2024. MHKiT (marine and hydrokinetic toolkit) - python.
- Kolmogorov, A.N., 1941. Dissipation of energy in the locally isotropic turbulence. In: *Dokl. Akad. Nauk. SSSR*. vol. 32, pp. 19–21.
- Lu, Y., Lueck, R.G., 1999. Using a broadband ADCP in a tidal channel, Part II: Turbulence. *J. Atmos. Ocean. Technol.* 16 (11), 1568–1579. [http://dx.doi.org/10.1175/1520-0426\(1999\)016<1568:UABAIA>2.0.CO;2](http://dx.doi.org/10.1175/1520-0426(1999)016<1568:UABAIA>2.0.CO;2).
- Lumley, J., Terray, E., 1983. Kinematics of turbulence convected by a random wave field. *J. Geophys. Res.* 13 (11), 2000–2007. [http://dx.doi.org/10.1175/1520-0485\(1983\)013<2000:KOTCBA>2.0.CO;2](http://dx.doi.org/10.1175/1520-0485(1983)013<2000:KOTCBA>2.0.CO;2).
- McCaffrey, K., Fox-Kemper, B., Hamlington, P.E., Thomson, J., 2015. Characterization of turbulence anisotropy, coherence, and intermittency at a prospective tidal energy site: Observational data analysis. *Renew. Energy* 76, 441–453. <http://dx.doi.org/10.1016/j.renene.2014.11.063>.
- McMillan, J.M., Hay, A.E., 2017. Spectral and structure function estimates of turbulence dissipation rates in a high-flow tidal channel using broadband ADCPs. *J. Atmos. Ocean. Technol.* 34 (1), 5–20. <http://dx.doi.org/10.1175/JTECH-D-16-0131.1>.
- McMillan, J.M., Hay, A.E., Lueck, R.G., Wolk, F., 2016. Rates of dissipation of turbulent kinetic energy in a high Reynolds number tidal channel. *J. Atmos. Ocean. Technol.* 33 (4), 817–837. <http://dx.doi.org/10.1175/JTECH-D-15-0167.1>.

- McVey, J., Kilcher, L., 2017. Velocity and turbulence measurements at three locations in the Salish Sea, WA, 2017. <http://dx.doi.org/10.15473/2476636>, [Dataset] <https://mhkdr.openei.org/submissions/563>.
- Mercier, P., Thiébaud, M., Guillou, S., Maisondieu, C., Poizot, E., Pieterse, A., Thiébot, J., Filipot, J.-F., Grondeau, M., 2021. Turbulence measurements: An assessment of acoustic Doppler current profiler accuracy in rough environment. *Ocean Eng.* 226, 108819. <http://dx.doi.org/10.1016/j.oceaneng.2021.108819>.
- Milne, I., Day, A., Sharma, R., Flay, R., 2016. The characterisation of the hydrodynamic loads on tidal turbines due to turbulence. *Renew. Sustain. Energy Rev.* 56, 851–864. <http://dx.doi.org/10.1016/j.rser.2015.11.095>.
- Milne, I., Sharma, R., Flay, R., 2017. The structure of turbulence in a rapid tidal flow. *Proc. R. Soc. A* 473 (2204), 20170295. <http://dx.doi.org/10.1098/rspa.2017.0295>.
- Milne, I.A., Sharma, R.N., Flay, R.G., Bickerton, S., 2013. Characteristics of the turbulence in the flow at a tidal stream power site. *Phil. Trans. R. Soc. A* 371 (1985), 20120196. <http://dx.doi.org/10.1098/rsta.2012.0196>.
- Mycek, P., Gaurier, B., Germain, G., Pinon, G., Rivoalen, E., 2014. Experimental study of the turbulence intensity effects on marine current turbines behaviour. Part I: One single turbine. *Renew. Energy* 66, 729–746. <http://dx.doi.org/10.1016/j.renene.2013.12.036>.
- National Oceanographic and Atmospheric Administration, 2015. NOAA current predictions. URL: <https://tidesandcurrents.noaa.gov/noaacurrents/>.
- Osalski, E., Side, J., Harris, R., 2009. Reynolds stress and turbulence estimates in bottom boundary layer of fall of warness. *Int. Commun. Heat Mass Transfer* 36 (5), 412–421. <http://dx.doi.org/10.1016/j.icheatmasstransfer.2009.02.004>.
- Ouro, P., Stoesser, T., 2019. Impact of environmental turbulence on the performance and loadings of a tidal stream turbine. *Flow Turbul. Combust.* 102, 613–639. <http://dx.doi.org/10.1007/s10494-018-9975-6>.
- Palodichuk, M., Polagye, B., Thomson, J., 2013. Resource mapping at tidal energy sites. *IEEE J. Ocean. Eng.* 38 (3), 433–446. <http://dx.doi.org/10.1109/JOE.2012.2227578>.
- Parker, B.B., 2007. *Tidal Analysis and Prediction*. NOAA, NOS Center for Operational Oceanographic Products and Services.
- Perez, L., Cossu, R., Grinham, A., Penesis, I., 2021. Seasonality of turbulence characteristics and wave-current interaction in two prospective tidal energy sites. *Renew. Energy* 178, 1322–1336. <http://dx.doi.org/10.1016/j.renene.2021.06.116>.
- Polagye, B., Thomson, J., 2013. Tidal energy resource characterization: methodology and field study in Admiralty Inlet, Puget Sound, WA (USA). *Proc. Inst. Mech. Eng. Part A: J. Power Energy* 227 (3), 352–367. <http://dx.doi.org/10.1177/0957650912470081>.
- Richard, J.-B., Thomson, J., Polagye, B., Bard, J., 2013. Method for identification of Doppler noise levels in turbulent flow measurements dedicated to tidal energy. *Int. J. Mar. Energy* 3, 52–64. <http://dx.doi.org/10.1016/j.ijome.2013.11.005>.
- Richmond, M., Harding, S., Romero-Gomez, P., 2015. Numerical performance analysis of acoustic Doppler velocity profilers in the wake of an axial-flow marine hydrokinetic turbine. *Int. J. Mar. Energy* 11, 50–70. <http://dx.doi.org/10.1016/j.ijome.2015.05.004>.
- Sentchev, A., Thiébaud, M., Schmitt, F.G., 2020. Impact of turbulence on power production by a free-stream tidal turbine in real sea conditions. *Renew. Energy* 147, 1932–1940. <http://dx.doi.org/10.1016/j.renene.2019.09.136>.
- Sutherland, D.A., MacCready, P., Banas, N.S., Smedstad, L.F., 2011. A model study of the Salish Sea estuarine circulation. *J. Phys. Oceanogr.* 41 (6), 1125–1143. <http://dx.doi.org/10.1175/2011JPO4540.1>.
- Thiébaud, M., Filipot, J.-F., Maisondieu, C., Damblans, G., Jochum, C., Kilcher, L.F., Guillou, S., 2020. Characterization of the vertical evolution of the three-dimensional turbulence for fatigue design of tidal turbines. *Phil. Trans. R. Soc. A* 378 (2178), <http://dx.doi.org/10.1098/rsta.2019.0495>.
- Thomson, J., Polagye, B., Durgesh, V., Richmond, M.C., 2012. Measurements of turbulence at two tidal energy sites in Puget Sound, WA. *IEEE J. Ocean. Eng.* 37 (3), 363–374. <http://dx.doi.org/10.1109/JOE.2012.2191656>.
- Thomson, J., Polagye, B., Richmond, M., Durgesh, V., 2010. Quantifying turbulence for tidal power applications. In: *OCEANS 2010. MTS/IEEE*, pp. 1–8. <http://dx.doi.org/10.1109/OCEANS.2010.5664600>.
- Thomson, J., Talbert, J., De Klerk, A., Zippel, S., Guerra, M., Kilcher, L., 2015. Turbulence measurements from moving platforms. In: 2015 IEEE/OES Eleventh Current, Waves and Turbulence Measurement. *IEEE*, pp. 1–5. <http://dx.doi.org/10.1109/CWTM.2015.7098107>.
- Welch, P., 1967. The use of fast Fourier transform for the estimation of power spectra: A method based on time averaging over short, modified periodograms. *IEEE Trans. Audio Electroacoust.* 15 (2), 70–73. <http://dx.doi.org/10.1109/TAU.1967.1161901>.
- Williams, E., Simpson, J.H., 2004. Uncertainties in estimates of Reynolds stress and TKE production rate using the ADCP variance method. *J. Atmos. Ocean. Technol.* 21 (2), 347–357. [http://dx.doi.org/10.1175/1520-0426\(2004\)021<0347:UIEORS>2.0.CO;2](http://dx.doi.org/10.1175/1520-0426(2004)021<0347:UIEORS>2.0.CO;2).
- Yang, Z., García-Medina, G., Wu, W.-C., Wang, T., Leung, L.R., Castrucci, L., Mauger, G., 2019. Modeling analysis of the swell and wind-sea climate in the Salish Sea. *Estuar. Coast. Shelf Sci.* (ISSN: 0272-7714) 224, 289–300. <http://dx.doi.org/10.1016/j.ecss.2019.04.043>.
- Yang, Z., Wang, T., 2013. Tidal residual eddies and their effect on water exchange in Puget Sound. *Ocean. Dyn.* 63, 995–1009. <http://dx.doi.org/10.1007/s10236-013-0635-z>.
- Yang, Z., Wang, T., Branch, R., Xiao, Z., Deb, M., 2021. Tidal stream energy resource characterization in the Salish Sea. *Renew. Energy* 172, 188–208. <http://dx.doi.org/10.1016/j.renene.2021.03.028>.